

RESEARCH ARTICLE

10.1029/2019MS001608

Key Points:

- A new, random force perturbations method was developed based on the cell perturbation method for turbulence generation
- Vertical force perturbations produce the shortest fetch for both neutral and convective stability conditions
- The force perturbations produced a fetch comparable to the cell perturbation method for neutral stability conditions

Correspondence to:

L. J. Mazzaro,
laura.mazzaro@gmail.com

Citation:

Mazzaro, L. J., Koo, E., Muñoz-Esparza, D., Lundquist, J. K., & Linn, R. R. (2019). Random force perturbations: A new extension of the cell perturbation method for turbulence generation in multiscale atmospheric boundary layer simulations. *Journal of Advances in Modeling Earth Systems*, 11, 2311–2329. <https://doi.org/10.1029/2019MS001608>

Received 23 JAN 2019

Accepted 31 MAY 2019

Accepted article online 6 JUN 2019

Published online 20 JUL 2019

Random Force Perturbations: A New Extension of the Cell Perturbation Method for Turbulence Generation in Multiscale Atmospheric Boundary Layer Simulations

L. J. Mazzaro^{1,2} , E. Koo² , D. Muñoz-Esparza³ , J. K. Lundquist¹ , and R. R. Linn²

¹Department of Atmospheric and Oceanic Sciences, University of Colorado Boulder, Boulder, CO, USA, ²Los Alamos National Laboratory, Los Alamos, NM, USA, ³National Center for Atmospheric Research, Boulder, CO, USA

Abstract Coupling between mesoscale and large eddy simulation (LES) is critically important for many atmospheric model applications, from predictions of wind energy to fire propagation. The grid-nesting technique enables bridging between vastly different scales without incurring prohibitive computational costs. However, the transition from coarser to finer resolutions often requires a large number of grid points from inflow boundaries for the development of fine-scale turbulence features in the LES domain. Recently, the cell perturbation method (CPM) was developed to reduce the turbulence development region with high computational efficiency. Herein, we explore a new method based on the CPM that uses force perturbations in both the horizontal and vertical directions (Force Cell Perturbation Method) instead of the potential temperature perturbations in the original CPM, as an attempt to further explore the performance of the random perturbation techniques. This approach is tested for a neutral and a convective atmospheric boundary layer under idealized conditions. Overall, similar performance is found between the optimal configurations of the CPM and the Force Cell Perturbation Method pointing to the robustness of this family of perturbation methods in accelerating turbulence generation in nested domains. Vertical force perturbations performed better than horizontal force perturbations for both atmospheric stability conditions. The CPM performed best under convective stability conditions. The combination of the force and potential temperature perturbations is found to provide no additional performance improvement over the stand-alone application of the individual methods.

1. Introduction

The prediction of wind energy production, fire propagation, and pollutant transport depends directly on both the large and small scales of the atmospheric flows in which these processes take place. Unfortunately, these flows are characterized by high Reynolds numbers, and simultaneously modeling such broad ranges of scales is computationally prohibitive and requires multiscale modeling techniques. A significant challenge with multiscale modeling is that high-resolution regions coupled with coarser-resolution forcing do not lead to instantaneous turbulence generation. Even with high resolution (~10 m) in large eddy simulation (LES) domains, an excessively large modeled area is necessary for fine-scale turbulence to develop (~10–30 km) (Mazzaro et al., 2017; Mirocha et al., 2014; Muñoz-Esparza et al., 2014, 2014; Tabor & Baba-Ahmadi, 2010; Zajaczkowski et al., 2011). Turbulence generation methods address this problem by shortening the distance necessary for the turbulent motions to develop. Here we present a modification to the cell perturbation method (CPM; Muñoz-Esparza et al., 2014, 2015; Muñoz-Esparza & Kosović, 2018), a technique for turbulence generation that uses random potential temperature perturbations to trigger small-scale motions near nested domain inflow boundaries. This new method variation uses random forces instead of potential temperature variations to trigger small-scale motions. By directly utilizing forces instead of temperature variations we test the robustness of the random perturbation methods, explore a more direct method for turbulence generation, and evaluate the advantages of applying the perturbations independently in different directions.

Due to the wide range of scales of motion contained in the atmosphere, it is computationally challenging to model certain atmospheric processes. For example, in order to represent all the scales of motion relevant to energy production from a wind farm, one may have to perform a simulation on a large enough domain

©2019. The Author.

This is an open access article under the terms of the Creative Commons Attribution-NonCommercial-NoDerivs License, which permits use and distribution in any medium, provided the original work is properly cited, the use is non-commercial and no modifications or adaptations are made.

(~100 km or more) to resolve the mesoscale structures of the atmosphere, while simultaneously using a fine enough grid point size (~1–5 m) to resolve the microscale characteristics of the wind turbine wakes (Archer et al., 2013; Bhaganagar & Debnath, 2014; Vanderwende et al., 2016; Vollmer et al., 2015). In this way, high-resolution turbulence statistics can be more accurately modeled by considering the mesoscale structures that affect the local planetary boundary layer (PBL) structure. While simulations of similar scale have been performed (Fang & Porté-Agel, 2015; Matheou et al., 2011; Seifert & Heus, 2013), they are very costly. For many applications, even larger domains would be necessary to capture the relevant mesoscale flows. Simulating such domains often requires prohibitively costly computational resources.

One solution to this computational cost issue has been to use homogeneous initial conditions for LES domains, where the initial conditions can be obtained from measurements or precursor mesoscale simulations, measurements, or forecast reanalysis. The LES domain is then allowed to develop the finer scales of motion through a spin-up period, using periodic boundary conditions (Deardorff, 1972, 1980; Moeng & Sullivan, 1994; Moeng & Wyngaard, 1994; Muñoz-Esparza et al., 2016; Smith & Skyllingstad, 2009; Sauer et al., 2016). This approach is appropriate if the microscale domain is smaller than the size of the mesoscale heterogeneities, in which case a homogeneous forcing is a reasonable approximation. However, for the case of LES over highly resolved domains that are larger than these mesoscale heterogeneities, homogeneous boundaries are no longer an accurate representation of the heterogeneous forcing. For example, LES over very large domains (Schalkwijk et al., 2015) may resolve heterogeneous, mesoscale weather patterns, while complex terrain (Sauer et al., 2016) can produce complex heterogeneities with a wide range of scales (Chow et al., 2019).

In response to this problem, different mesoscale-to-microscale model coupling strategies are being explored. One such strategy is the grid-nesting method (Jähn et al., 2016; Liu et al., 2011; Mazzaro et al., 2017; Mirocha et al., 2014; Muñoz-Esparza et al., 2015, 2017; Rai et al., 2016; Talbot et al., 2012; Zhou & Chow, 2013). Through this method, mesoscale flows are modeled over large, coarsely resolved domains, the solution of which is then used as boundary conditions to smaller, highly resolved, microscale domains that are strategically located around an area of interest. This approach enables modeling of a wide range of scales, while considering mesoscale heterogeneities without incurring the enormous computational costs required by a single-domain simulation.

An issue with the aforementioned grid-nesting method is the cost of noninstantaneous microscale turbulence development: a significant portion of the microscale domain, or "fetch," is necessary for the low-turbulence boundary conditions to fully develop microscale turbulence (Tabor & Baba-Ahmadi, 2010; Zajaczkowski et al., 2011; Mirocha et al., 2014; Muñoz-Esparza et al., 2014, 2014). For a microscale simulation performed at a grid point resolution of 50 m, this required fetch can exceed 30 km (Muñoz-Esparza et al., 2014; Mazzaro et al., 2017). Therefore, additional techniques are necessary to accelerate the development of microscale turbulence and thus avoid excessive computational costs incurred by such large fetch.

Several approaches to minimizing this fetch are in use. All of these methods have certain advantages and drawbacks, but so far, none performs optimally for all applications. Preprepared methods (Keating et al., 2014; Lee et al., 1992) use an auxiliary simulation to generate turbulence with the desired forcing. The turbulence generated is then imposed at the inflow boundary of the domain of interest, immediately satisfying the equations of motion and minimizing turbulence development fetch. However, this method may contain spurious periodicity and requires performing a separate simulation, with the same domain size and resolution as the domain of interest, making it an expensive option.

Recycling methods (Araya et al., 2011; Keating et al., 2014; Mayor et al., 2002; Morgan et al., 2011; Nakayama et al., 2012) can eliminate the auxiliary domain requirement from preprepared methods. They extract the solution of the downstream section of the domain of interest and reinsert it at its inlet. This turbulence can be rescaled using similarity laws (Lund et al., 1998). This method has been successfully tested for plane-channel flow (Araya et al., 2011; Morgan et al., 2011; Nakayama et al., 2012). However, for atmospheric applications, in which flow direction is variable in time, or where there are multiple inflow boundaries, the implementation of this method becomes very complex.

The preprepared and recycling methods allow turbulence to be developed naturally by the model, reusing turbulence generated by the model to accelerate the process. An alternative to these is the forcing method (Keating et al., 2014; Spille-Kohoff & Kaltenbach, 2001; Zajaczkowski et al., 2011), which applies

wall-normal forcing at the domain inlet, driving the flow to develop a desired Reynolds shear stress. The forcing method generates turbulence faster than the preprepared and recycling methods. However, even with these improvements, computational costs remain very high (Keating et al., 2014), which is why these methods are not currently used. Additionally, the forcing method requires detailed, a priori knowledge of the desired turbulence, which is most often not available, and would thus require performing an additional simulation.

Another class of turbulence generation techniques, the synthetic turbulence methods, create a turbulent velocity field that reproduces certain target turbulence statistics (Le et al., 1997; Pames et al., 2009). With the use of digital filtering techniques, these methods can generate turbulence that reproduces prescribed Reynolds stresses (di Mare et al., 2006; Klein et al., 2003; Xie & Castro, 2008). Although promising, these methods present many disadvantages: the synthetic turbulent velocity fields generated are often not divergence-free (Kondo et al., 1997; Poletto et al., 2013), still require long fetches for the turbulence to develop, and require significant information about the statistics of the target turbulence.

The previous methods require a significant level of a priori knowledge about the target turbulence, as well as a long fetch to allow the turbulence to develop. In response to these drawbacks, a new class of methods, the random perturbation methods, have been explored in recent years. Their goal is to generate random, small-scale shear at the domain inflow boundaries to stimulate the development of turbulence in order to decrease the turbulence generation fetch. The idea of triggering turbulent motions near the nested domain inflow boundaries was first explored by Mirocha et al. (2014), who tested the effects of adding forces with sinusoidal amplitudes to the temperature and velocity field inflow boundaries, finding promising results. Muñoz-Esparza et al. (2014, 2015) and Muñoz-Esparza and Kosović (2018) further advanced the perturbation method by using random, instead of sinusoidal, θ perturbations, as well as introducing perturbation cells specifically designed to account for implicit filtering inherent to the advection discretization schemes typically used in numerical weather prediction models. This method is minimally dependent on the target turbulence and instead can be based on the large-scale PBL conditions, making it a cost-effective option that is applicable to a broader range of implementations, such as time-variable cases (Jähn et al., 2016; Muñoz-Esparza & Kosović, 2018) and complex terrain (Jähn et al., 2016). Muñoz-Esparza et al. (2015) and Muñoz-Esparza and Kosović (2018) developed stability-aware scalings for the amplitude of the potential temperature perturbations under neutral stability conditions, showing vast improvements over alternative techniques. However, despite this optimization, turbulence generation fetches continue to constitute a significant fraction of computational expenses: in some situations, fetches on the order of 30 km, with grid point resolutions as low as 50 m, are necessary for the proper turbulence scales to develop (Mazzaro et al., 2017).

By perturbing the flow with direct forces, rather than through temperature gradients, we may apply different forcing in different directions which may improve performance for specific stability conditions. For example, we may expect that while the interaction of potential temperature perturbations and a CBL would allow for the perturbations to develop long-living unstable accelerations, while potential temperature perturbations over a more stable stratification (NBL or SBL) may get dampened by the background temperature gradient. Additionally, we expect an increase in the rate of turbulence generation due to the direct acceleration and deceleration of the flow through force perturbations. We also explore the combination of temperature and force perturbations, to test whether they complement each other for specific stability conditions. By testing this novel perturbation technique on idealized neutral (NBL) and convective (CBL) boundary layers, we evaluate its performance and make appropriate implementation recommendations.

This paper is structured as follows: Section 2 explains the implementation of the force perturbations; section 3 describes the numerical setup of our simulations; section 4 describes the force perturbation performance for a CBL and NBL; section 5 presents the effects of combining different perturbation techniques. Finally, in section 6 we summarize our insights and present the conclusions of this study.

2. The Force Perturbations

We developed the Force Cell Perturbation Method (FCPM) based on the CPM, by introducing random forces near the inflow boundaries of nested domains. With this new random perturbation method variation we test the strength of this class of turbulence generation techniques while exploring potential improvements to current implementations.

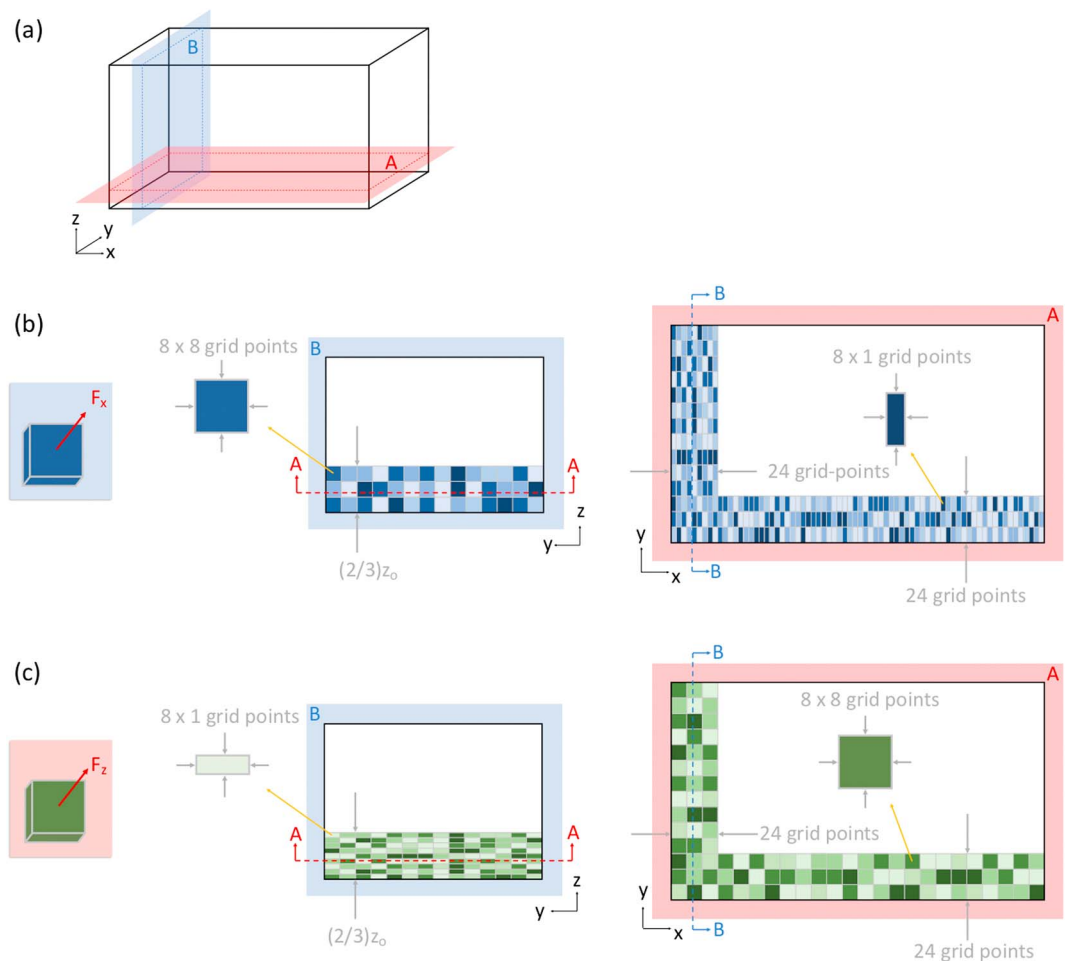


Figure 1. (a) Diagram showing the domain cross sections shown; (b) force perturbation structure in the x direction; (c) force perturbation structure in the z direction.

The FCPM is implemented by superimposing random perturbations to the Weather Research and Forecasting Model (WRF) momentum tendency fields (kg/s^4) near the nested inflow boundaries. This approach is equivalent to adding random accelerations and decelerations, or forces to the flow. The amplitude for each of these random forces is selected from a uniform distribution, which we define by a maximum perturbation value. Due to the mass-coupled configuration of the WRF transport equations, the conversion from force perturbation amplitude to equivalent acceleration follows a nonlinear relationship. The acceleration produced by a specific force perturbation amplitude will have an inverse dependence on the pressure from the modeled atmospheric column above the perturbed location. In this new method variation we perturb the scalar tendencies of the individual velocity components instead of directly perturbing the velocity components. In this way, we apply fluctuations that allow the model's equations of motion to compute the velocity variations. This is consistent with the mechanism used by the CPM, where the potential temperature variations are used by the model's equations of motion to accelerate and decelerate the flow.

As with the CPM, the force perturbations are applied over two-dimensional cells with a size of 8×8 grid points (Figures 1a–1c). This size was selected by Muñoz-Esparza et al. (2014) as the minimum necessary to avoid numerical dissipation effects that can weaken the perturbations before the full turbulent cascade can develop. The orientation of the perturbed cells is chosen to be perpendicular to the direction of the perturbing force (Figures 1b and 1c). For example, a force perturbing the x direction, F_x , (Figure 1b) will be applied over a cell of dimensions $[L_x, L_y, L_z] = [1, 8, 8]$ grid points, while a force perturbing the z direction, F_z , (Figure 1c) will be applied over $[8, 8, 1]$ grid points. We perturb a total of three cells or 24 grid points along each inflow boundary. In this study, the flow is from the southwest direction. We therefore perturb the southern and western boundaries of the nested LES domains.

Table 1
Domain Characteristics for the Two Stability Conditions in This Study, Including Horizontal Resolution (Δx , Δy), Vertical Resolution (Δz), Domain Size (L), and Spin-Up Times

| | | Δx , Δy | Δz | $[L_x, L_y, L_z]$ | Spin-up |
|--------------------|------------|-------------------------|------------|-------------------|---------|
| Parent (mesoscale) | Convective | 999 m | 20 m | [600, 600, 3] km | 4 hr |
| | Neutral | 270 m | 20 m | [58, 25, 1.5] km | 24 hr |
| Nest (LES) | Convective | 47.57 m | 20 m | [51, 21, 3] km | 4 hr |
| | Neutral | 30 m | 20 m | [54, 21, 1.5] km | 4 hr |

Note. LES = large eddy simulation.

The vertical extent of the FCPM was chosen to match the CPM. In the vertical direction, the CPM perturbs up to two thirds of the total boundary layer height, z_i . The top third of the boundary layer is not perturbed to avoid interactions between the θ fluctuations and the inversion layer (Muñoz-Esparza et al., 2015). The same structure is implemented for the force perturbations, which are only applied in the lower two thirds of the boundary layer. Additionally, horizontal force perturbations are applied independently in the x and y directions, to test whether the relationship between perturbation direction and the background stratification may produce improvements. For example, we may expect that vertical force perturbations will have a greater effect under convective stability conditions, where the background convective forcing could allow the perturbations to develop unstable motions, while horizontal perturbations may perform better under less unstable conditions, such as the NBL or the SBL, where vertical accelerations may be dampened by the background stability. Throughout the rest of this study we refer to the superposition of these horizontal perturbations as F_{xy} .

The entire perturbation field is refreshed after a period of time, t_d , calculated following the method described by Muñoz-Esparza et al. (2015), using dimensionless number, $\Gamma = t_d U_1 d_c^{-1} = 1.3$. In this equation, U_1 is the wind speed of the incoming flow at the lowest vertical level, and d_c is the diagonal grid point size.

3. Methodology

We use the WRF model version 3.6 (Skamarock et al., 2008) to test the FCPM through a series of idealized, one-way nested, mesoscale-to-LES simulations. We compare the performance of the FCPM to the CPM. All of our simulations consist of an LES domain, one-way nested within the center of a mesoscale domain. Perturbations are added to the LES inflow boundaries. For each stability condition, a separate, unperturbed simulation was used as a reference, to help quantify the improvements produced by the perturbations.

3.1. Simulations

The PBL scheme used for the mesoscale domains is the MYNN 2.5 scheme (Nakanishi & Niino, 2009). For the nested LES we used the nonlinear backscatter and anisotropy (NBA) scheme (Kosović, 1997), which was implemented in WRF by Mirocha et al. (2010). The surface layer was modeled using Monin-Obukhov similarity theory (Jimenez et al., 2012; Monin & Obukhov, 1954). Cloud physics, microphysics, radiation and land surface parameterizations are not used. Coriolis effects correspond to a coriolis frequency of $f = 9.97 \times 10^{-5} s^{-1}$, which is equivalent to a latitude of 43.3°N. All of the simulations were performed on a dry atmosphere, with flat terrain with a surface roughness z_0 of 0.1 m.

In this study we focus on testing the FCPM under two atmospheric stability conditions: neutral and convective. Table 1 shows the numerical domain setup for each of these conditions.

The parent, mesoscale resolutions is used to maintain a relatively low-grid refinement ratio (10–20), while still allowing for a fine enough resolution to partially resolve the inertial range of turbulence for the convective (~ 50 m) and neutral (~ 30 m) cases. For the convective stability conditions we use a higher grid refinement ratio than the neutral case, thus minimizing the amount of turbulent kinetic energy (TKE) present in the convective mesoscale forcing. The spin-up time for each domain is based on the temporal evolution of the modeled turbulence. Spin-up time is chosen to allow for the turbulence to reach a steady state. For every domain, resolved TKE, turbulent energy spectra, and turbulence variances are considered for this selection. The same vertical resolution was used for all simulations. A Raleigh damping layer with a coefficient of $0.2 s^{-1}$ is applied to the top 500 m of the neutral stability domains, and to the top 850 m for the

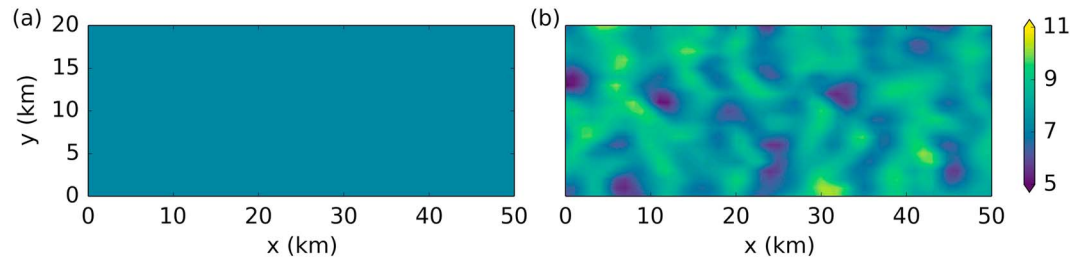


Figure 2. Instantaneous horizontal contours of wind speed in the x direction, u (m/s) at a height $0.2z_i$ for the periodic, mesoscale, parent domains, for the last simulated time frame. (a) Neutral boundary layer; (b) Convective boundary layer.

convective stability domains. Through this damping layer we ensure that turbulent motions do not reach the top boundary of the modeled domains (Klemp et al., 2008).

The CBL layer is forced by a surface sensible heat flux, $\langle w'\theta' \rangle_s = 0.08 \text{ K m s}^{-1}$, where the brackets, $\langle \rangle$, represent the expectation value, calculated using an ensemble average of the vertical wind speed and potential temperature fluctuations (w' and θ'). Both the NBL and CBL are initialized with a uniform temperature profile of 288 K. The top of the boundary layer is delimited by a 150-m deep temperature inversion layer of strength 0.08 K m s^{-1} , starting at height $z_i = 500 \text{ m}$ for the neutral case, and $z_i = 2,000 \text{ m}$ for the convective case. Above the inversion layer is a weaker inversion, with a strength of 0.003 K/m .

A geostrophic wind is applied in the x direction, with a magnitude of $(U_g, V_g) = (10, 0) \text{ m/s}$ for the neutral case, and $(U_g, V_g) = (8.1, 0) \text{ m/s}$ for the convective case. Due to Coriolis effects, after spin-up, the mean flow has both x and y components. We assess fetch in the x direction, but due to the diagonal direction of the incoming flow, the inflow through the boundary parallel to the y axis also requires fetch to develop turbulence. We use the evolution of TKE ($q = 0.5(\langle u'u' \rangle + \langle v'v' \rangle + \langle w'w' \rangle)$) with distance at two heights in the boundary layer ($0.2z_i$ and $0.5z_i$) to find that a fetch of $\sim 5 \text{ km}$ in the y direction is enough for the TKE to be near a steady value (within $\approx 10\%$). To remove the influence of the y direction fetch in our analysis, we do not consider data from within 5 km of the southern inflow boundary for nested domain calculations of flow statistics.

The mesoscale parent simulations for the NBL do not develop resolved turbulence due to their coarse resolution (Figure 2a). These mesoscale domains produce a homogeneous, neutral forcing for the nested LES simulations. However, for the convective case, the mesoscale simulations contain convective circulations

Table 2
List of Simulations Performed, Showing the Perturbation Method (Perturbation Units), Along With the Maximum Perturbation Amplitudes

| Label | NBL | | CBL | | |
|-------------------------|---|------------|--------------------------|---|--------------|
| | Method (units) | Amplitude | Label | Method (units) | Amplitude |
| N_{NP} | - | - | C_{NP} | - | - |
| $N_{\theta 0.35}$ | θ (K) | 0.35 | $C_{\theta 0.33}$ | θ (K) | 0.33 |
| N_{xy750} | | 750 | C_{xy1000} | | 1000 |
| N_{xy1000} | F_{xy} (kg/s ⁴) | 1,000 | C_{xy2000} | F_{xy} (kg/s ⁴) | 2,000 |
| N_{xy1250} | | 1,250 | C_{xy5000} | | 5,000 |
| N_{z1000} | | 1,000 | C_{z1500} | | 1,000 |
| N_{z1250} | F_z (kg/s ⁴) | 1,250 | C_{z5000} | F_z (kg/s ⁴) | 5,000 |
| N_{z1500} | | 1,500 | C_{z10000} | | 10,000 |
| $N_{\theta 0.25+xy500}$ | θ (K), F_{xy} (kg/s ⁴) | 0.25, 500 | $C_{\theta 0.16+xy1500}$ | θ (K), F_{xy} (kg/s ⁴) | 0.16, 1,500 |
| $N_{\theta 0.5+xy1000}$ | | 0.5, 1,000 | $C_{\theta 0.33+xy500}$ | | 0.33, 5,000 |
| $N_{\theta 0.25+z750}$ | θ (K), F_z (kg/s ⁴) | 0.25, 750 | $C_{\theta 0.16+z5000}$ | θ (K), F_z (kg/s ⁴) | 0.16, 5,000 |
| $N_{\theta 0.5+z1250}$ | | 0.5, 1,250 | $C_{\theta 0.33+z10000}$ | | 0.33, 10,000 |

Note. NBL = neutral boundary layer; CBL = convective boundary layer.

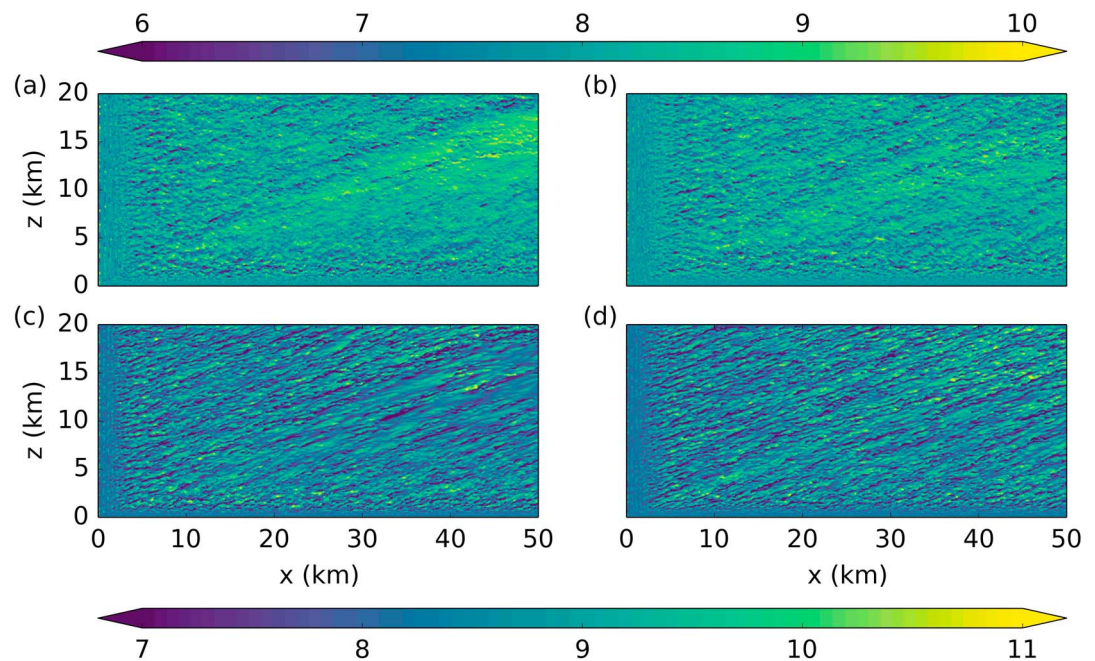


Figure 3. Instantaneous horizontal contours of wind speed in the x direction, u (m/s), at a height of (a, b) $0.5z_i = 250$ m and (c, d) $0.2z_i = 100$ m, for (a, c) $\bar{\theta}_{pm} = 0.50$ K and (b, d) $\bar{\theta}_{pm} = 0.35$ K. Contours are for the last simulated time frame in the neutral boundary layer. The top color bar corresponds to figures (a) and (b), the bottom color bar corresponds to figures (c) and (d).

with low levels of turbulence, despite their relatively coarse resolution (Figure 2b). These structures are explained by the effects of the use of terra incognita (TI; Wyngaard, 2004) resolutions. The length scale of the convective structures that would result from the convective forcing in these simulations is on the same order as the mesoscale resolution used in this study. Because of this, certain structures are partially resolved, resulting in the presence of resolution-dependent flow heterogeneities, along with other unrealistic characteristics (Beare, 2013; Ching et al., 2014; Honnert et al., 2011; Shin & Dudhia, 2016; Zhou et al., 2014). These unrealistic flows have been studied in the context of mesoscale-to-LES grid nesting (Mazzaro et al., 2017): although their effect can influence the rate of evolution of turbulence, they do not produce a significant bias in the turbulence observed past the development portion of the domain. While these TI structures can be avoided through certain setup modifications (Muñoz-Esparza et al., 2017), such alterations are not widely used, and the acceleration of turbulence generation starting from such heterogeneous TI flows rather than smooth flows remains an important problem, and it is addressed in this study.

3.2. Random Force Perturbation Method (FCPM)

The goal of this study is to test and optimize the performance of the FCPM under two different stability conditions. We test different values of the maximum vertical and horizontal force perturbation amplitude.

Table 2 shows the amplitudes selected for the neutral and convective stability conditions. The horizontal combination of force perturbations in the x and y directions was chosen to test whether there are significant effects due to the interaction of stability and general perturbation directions. However, further analysis of the horizontal FCPM could include separate comparisons between perturbations in the x and y directions. As described in section 2, t_d was selected to be 64 s for the neutral case, and 23 s for the convective case.

Turbulence generation fetch is evaluated through resolved TKE and turbulent spectra ($k_y F_{wy}$, $k_y F_{wy}$, and $k_y F_{vy}$). While we do not use a quantitative threshold to determine the exact turbulence generation fetch, our main criteria for fetch estimation is that TKE must be stabilized or

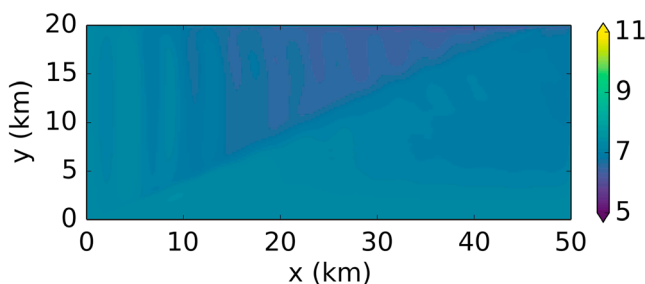


Figure 4. Instantaneous horizontal contour of wind speed in the x direction, u (m/s) at a height $0.2z_i \approx 100$ m for N_{NP} , for the last simulated time frame.

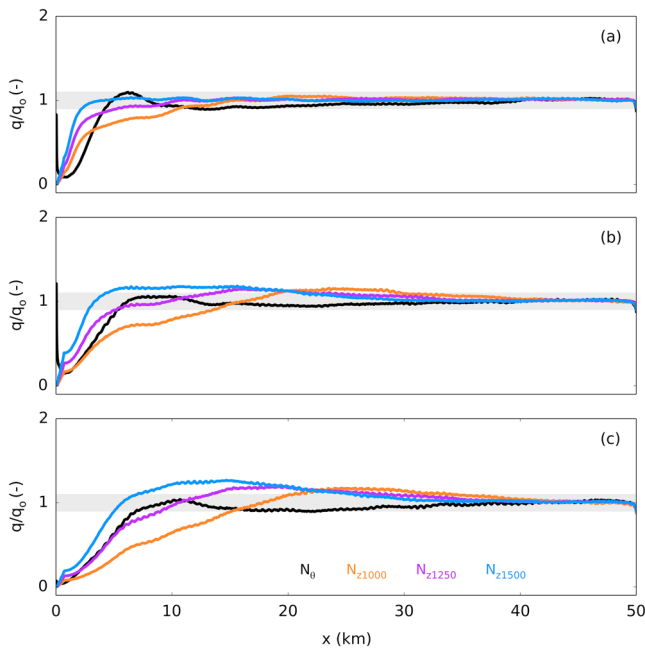


Figure 5. Neutral boundary layer evolution of time-averaged, resolved turbulent kinetic energy (q), for the nested large eddy simulation forced with F_z perturbations, as a function of distance downstream of the nested inflow boundary, x , at heights (a) 100, (b) 250, and (c) 350 m. At each height, q is normalized by q_0 , the mean of turbulent kinetic energy at $x = 40$ to 50 km for that specific height.

asymptotically approaching a constant value. By comparing the evolution of turbulence between the different tested configurations we find the optimal amplitude for both the vertical and horizontal force perturbations, producing the shortest fetch.

3.3. Potential Temperature Perturbation Method (CPM)

Once the ideal maximum amplitude is identified for each force perturbation direction and stability condition, as described in section 2, the FCPM is compared to an optimal application of the CPM.

To find this optimal CPM amplitude, we first select the maximum perturbation value ($\tilde{\theta}_{pm}$). This value characterizes the optimal uniform distribution from which the random values are drawn. An initial guess for $\tilde{\theta}_{pm}$ in NBL conditions is determined by the perturbation Eckert number, such that $Ec = U_g^2(c_p \tilde{\theta}_{pm})^{-1} \approx 0.2$ (Muñoz-Esparza et al., 2015), where $c_p \approx 1.005$ kJ/(kg K) is the specific heat capacity of dry air at constant pressure. Based on this criterion, we selected an initial $\tilde{\theta}_{pm} = 0.50$ K for the NBL. Using the same method, we selected $\tilde{\theta}_{pm} = 0.33$ K for the CBL. A new optimized scaling for convective stability conditions was recently developed by Muñoz-Esparza et al. (2018), and we expect that the use of their new development for the convective stability case could result in potential improvements to the CPM performance documented herein, which has been based on the perturbation Eckert number.

For the NBL, the initially selected $\tilde{\theta}_{pm} = 0.50$ K produced a diagonal region of higher velocities for a height of $z = 0.5z_i$ (Figure 3a), and weaker fluctuations in the same diagonal region at a lower height of $z = 0.2z_i$ (Figure 3c). The presence of this diagonal pattern is consistent with observations of other CPM simulations in which suboptimal perturbation amplitudes were used (Figure 1 from Muñoz-Esparza et al., 2015). To reduce this effect and better optimize the CPM amplitudes in the current configuration, we tested different $\tilde{\theta}_{pm}$ values and found that a

diagonal pattern is consistent with observations of other CPM simulations in which suboptimal perturbation amplitudes were used (Figure 1 from Muñoz-Esparza et al., 2015). To reduce this effect and better optimize the CPM amplitudes in the current configuration, we tested different $\tilde{\theta}_{pm}$ values and found that a

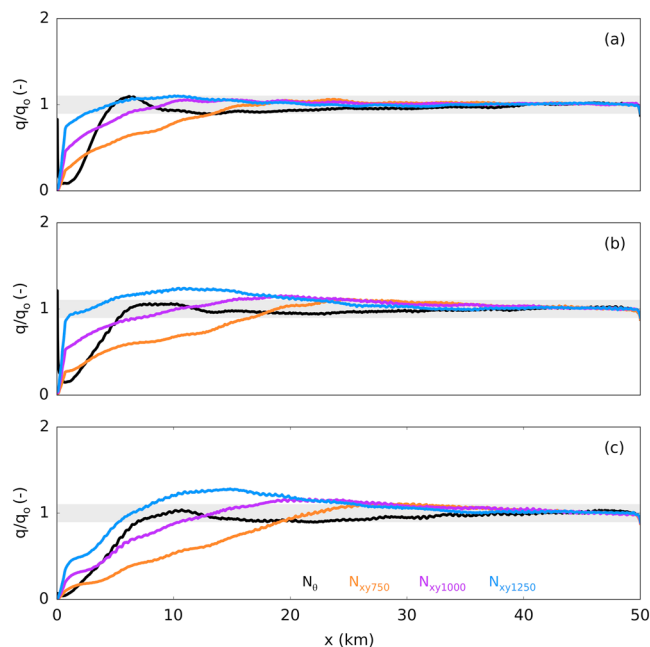


Figure 6. Neutral boundary layer evolution of time-averaged, resolved turbulent kinetic energy (q), for the nested large eddy simulation forced by F_{xy} perturbations, as a function of distance downstream of the nested inflow boundary, x , at heights (a) 100, (b) 250, and (c) 350 m. At each height, q is normalized by q_0 , the mean of turbulent kinetic energy at $x = 40$ to 50 km for that specific height.

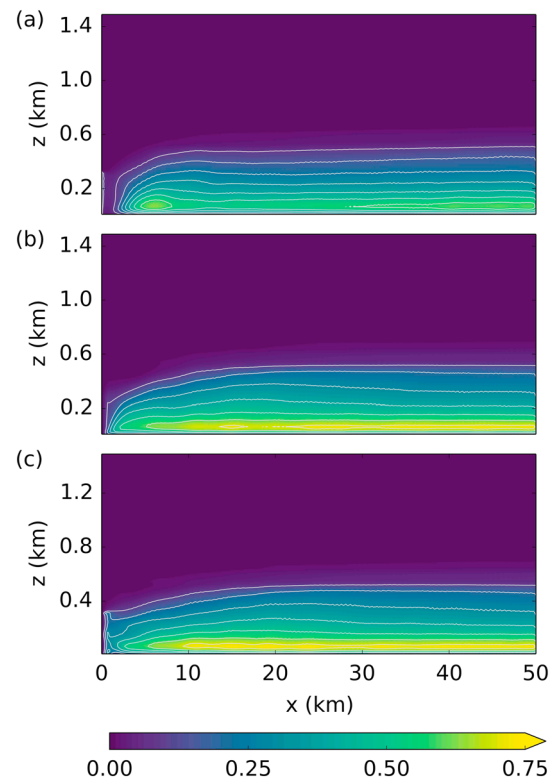


Figure 7. Evolution of y -averaged turbulent kinetic energy, q (m^2/s^2), (a) $N_{\theta 0.5}$, (b) N_{z1250} , and (c) N_{xy1000} , as a function of distance downstream of the inflow boundary, x , for the last simulated timestep. The white lines represent constant TKE contours.

value of $\tilde{\theta}_{pm} = 0.35$ K eliminated these patterns almost entirely (Figures 3b and 3d), while being high enough to maintain the short turbulent generation fetch of the CPM. This value was selected as the optimal perturbation amplitude for our setup and used to compare between the CPM and FCPM throughout the rest of this study. At this time, it is unclear why the optimal perturbation Eckert number estimated by Muñoz-Esparza et al. (2015) does not produce the expected results in this simulation, but differences between WRF version 3.6 and other versions may have played a role in this variation.

Additionally, we examine the effect of combining the CPM with vertical and horizontal force perturbations. For this, we perturb the nested domain with two methods, simultaneously. Two different perturbation combination configurations are tested. In the first combination case, the perturbation amplitude of each method is chosen to be approximately half of its optimal value. For the second case, the full optimal amplitudes are combined. In this way, we begin to explore the potential advantages of allowing interactions between the structures generated by these techniques.

4. Results

4.1. Neutral Stability Conditions

Neutral LES were forced by homogeneous mesoscale flows (Figure 2a). Therefore, the inflow boundaries of the neutral LES domains contain no resolved TKE. Starting from these smooth inflow conditions, the unperturbed, nested LES did not develop significant levels of turbulence (Figure 4).

By comparing the evolution of 3-hr averaged, resolved TKE for the perturbation strengths shown in Table 2, we select optimal force perturbation amplitudes for the two stability cases in this study. This optimal value represents the configuration that reaches an asymptotic TKE value in the shortest fetch. For both perturbation directions (vertical: Figure 5 and horizontal: Figure 6) TKE increases rapidly, then evolves more slowly before stabilizing at an asymptotic value. When perturbation amplitudes exceed the optimal value, higher heights show a slow increase of TKE above the asymptotic value, before decreasing and stabilizing. An example of this is seen for N_{z1500} (Figure 5). However, for weaker perturbation amplitudes, TKE cannot

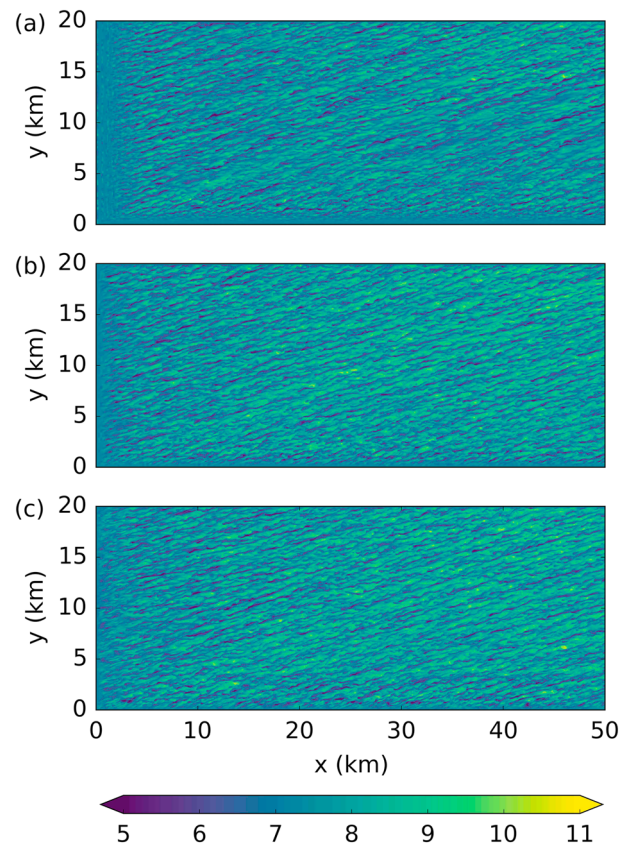


Figure 8. Instantaneous horizontal contours of wind speed in the x direction, u (m/s), at a height $0.5z_i \approx 100$ m, at the end of the measurement period, for (a) $N_{\theta,0.35}$, (b) $N_{z,1250}$, and (c) $N_{xy,1000}$.

increase above the asymptotic value and instead increases slowly from zero, over a longer distance, as seen in $N_{z,1000}$. Additionally, the CPM shows a large TKE peak at the inflow boundaries, for heights within the perturbed layer (Figures 5a and 5b). This peak quickly dissipates, and TKE drops dramatically before slowly increasing again toward convergence. This dramatic evolution of TKE near the inflow boundary indicates that the sharp potential temperature gradients between perturbations produce high levels of TKE that are quickly smoothed out by local mixing, before a slower evolution process takes place. At low heights of 100 m (Figure 5a), $N_{z,1500}$ produces fetches as short as 5 km, while the CPM produces a fetch closer to 10 km. However, at 250 and 350 m $N_{z,1500}$ perturbations produce high TKE overshoots that take a longer distance to dissipate, while $N_{z,1250}$ produces shorter fetches of 10–15 km, which are comparable to $N_{\theta,0.35}$. Based on these observations, $N_{z,1250}$ and $N_{xy,1000}$ were selected as the optimal configurations for each perturbation direction, and $N_{z,1250}$ produced the overall best FCPM performance, with fetches comparable to the CPM at all heights.

While Figures 5 and 6 allow for comparisons at a few specific heights within the BL, Figure 7 shows a comparison of resolved TKE for all heights, for the three optimized perturbation configurations ($N_{\theta,0.35}$, $N_{z,1250}$, and $N_{xy,1000}$). Figure 13c shows that F_{xy} have a stronger, immediate effect on TKE, which can be observed near $x = 0$ m. The force perturbations (Figures 7b and 7c) trigger higher final levels of turbulence near the surface, while the θ perturbations (Figure 7a) produce levels of turbulence that are significantly lower in this region. Horizontal contours of horizontal wind speed, u (Figure 8) show visibly weaker fluctuations throughout the domain for the CPM case at a height of 100 m. These differences are not taken into account when calculating turbulence generation fetch.

Although assessment of resolved TKE values provides a general picture of the turbulence generation process, the analysis of the turbulence spectra of u , w , and v demonstrates how the length scales generated by each perturbation configuration differ, and how they evolve to their final levels. The evolution of these three variables for the three perturbation methods analyzed appears in Figure 9. For the first 3 km downstream of the inflow boundary, all three spectra components develop fastest for the horizontal FCPM ($N_{xy,1000}$).

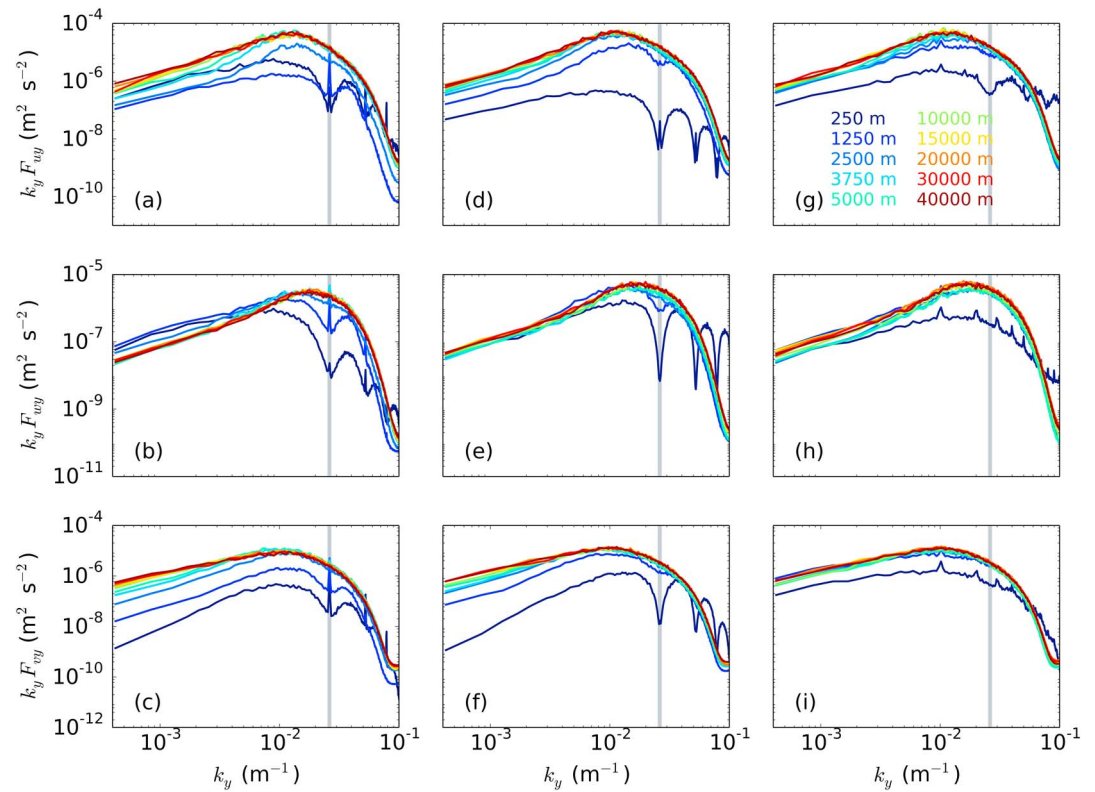


Figure 9. Time-averaged turbulent spectra of u , w , and v in the y direction for (a–c) $N_{\theta 0.35k}$, (d–f) N_{z1250} , and (g–i) N_{xy1000} , as a function of wave number, k_y , at a height of 100 m. The vertical gray lines show the wave number corresponding to the scale of the perturbations ($8 \Delta x$).

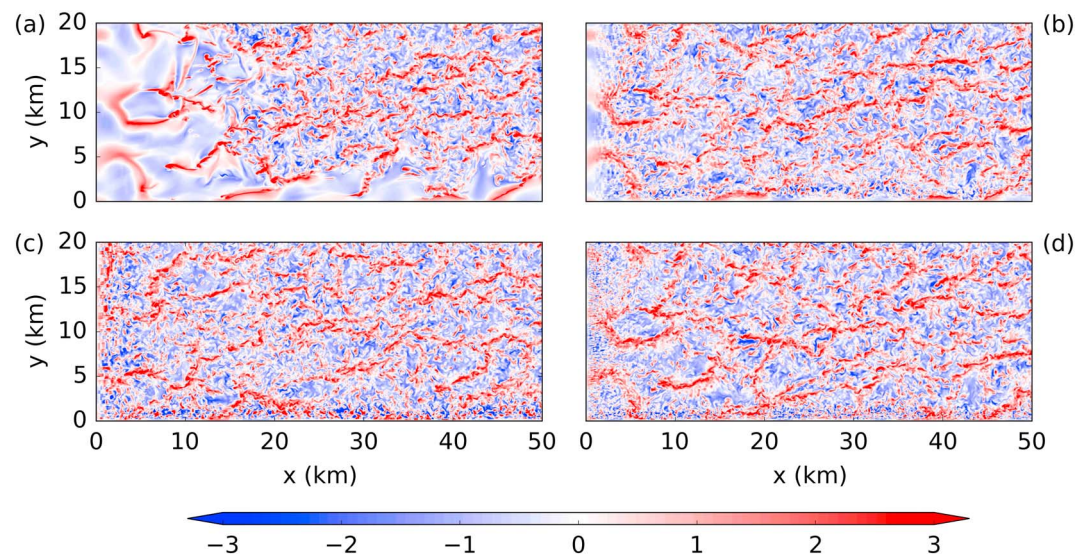


Figure 10. Instantaneous horizontal contours of wind speed in the z direction, w (m/s), at a height $0.5z_i \approx 400$ m, and at the end of the simulation period, for (a) C_{NP} , (b) $C_{\theta 0.35}$, (c) C_{z10000} , and (d) C_{xy5000} .

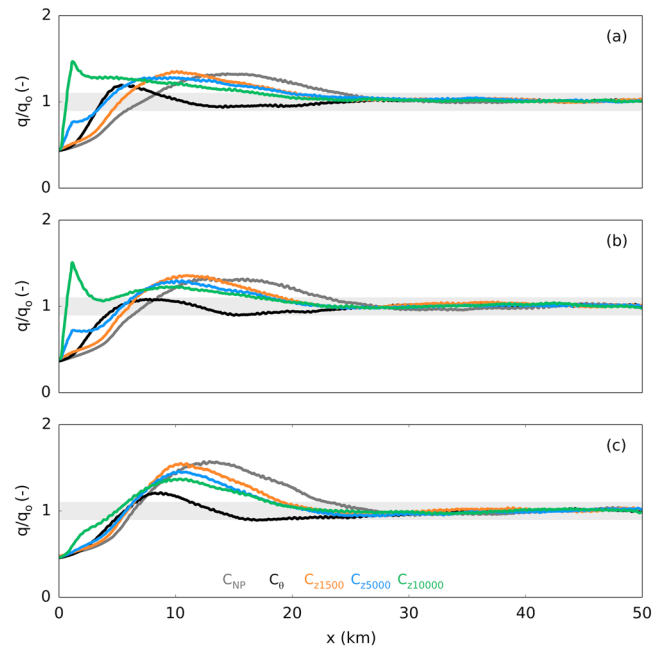


Figure 11. Convective boundary layer evolution of time-averaged, resolved turbulent kinetic energy (q), for the nested large eddy simulation forced by F_z perturbations, as a function of distance downstream of the nested inflow boundary, x , at heights (a) 500, (b) 1,000, and (c) 1,500 m. At each height, q is normalized by q_0 , the mean of TKE at $x = 40$ to 50 km for that specific height.

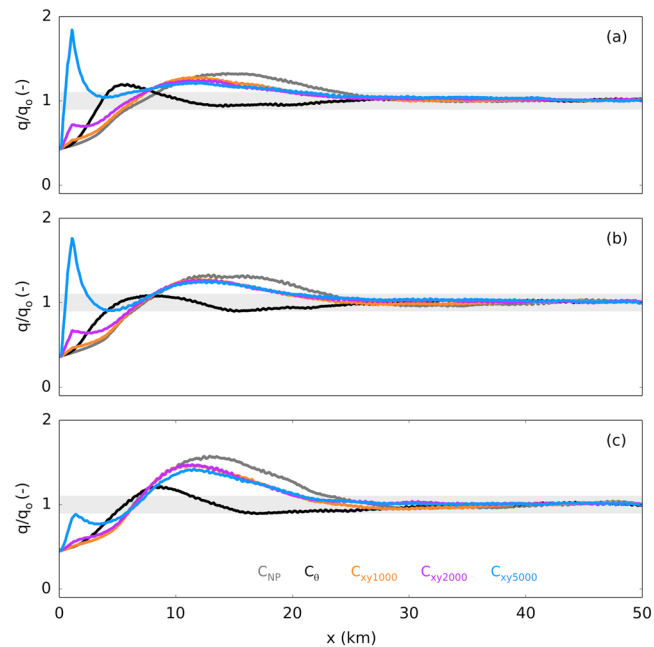


Figure 12. Convective boundary layer evolution of time-averaged, resolved turbulent kinetic energy (q), for the nested large eddy simulation forced by F_{xy} perturbations, as a function of distance downstream of the nested inflow boundary, x , at heights (a) 500, (b) 1,000, and (c) 1,500 m. At each height, q is normalized by q_0 , the mean of TKE at $x = 40$ to 50 km for that specific height.

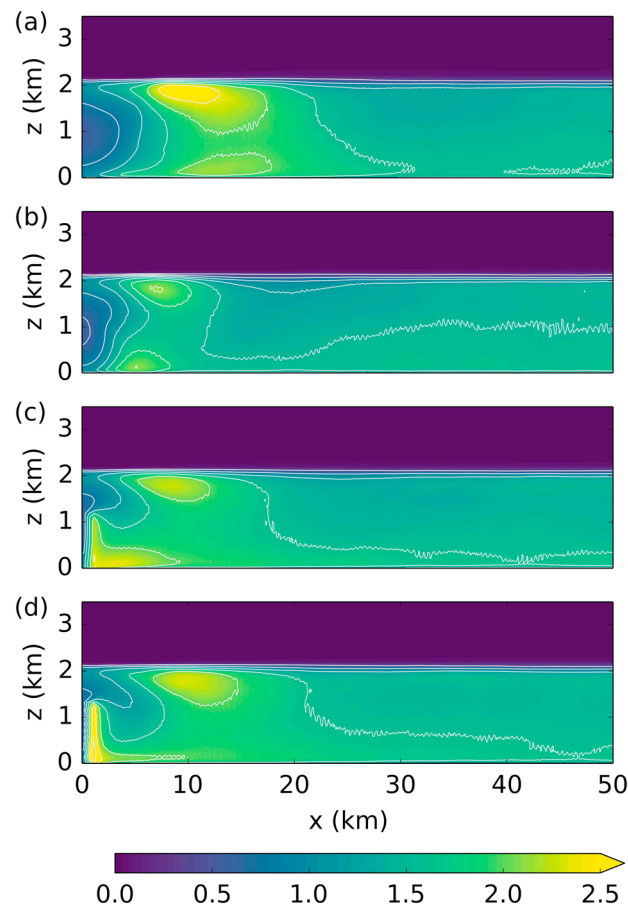


Figure 13. Evolution of y -averaged turbulent kinetic energy, q (m^2/s^2), (a) C_{NP} , (b) $C_{\theta 0.33K}$, (c) C_{z10000} , and (d) C_{xy5000} , as a function of distance downstream of the inflow boundary, x , for the last simulated time step. The white lines represent constant turbulent kinetic energy contours.

This faster initial development is consistent with TKE observations (Figure 7). This initial development is slowest for the CPM. Farther downstream we observe different behavior for high and low wave numbers. For high wave numbers ($k_y > 0.004 \text{ m}^{-1}$), the CPM reaches a more stable equilibrium faster than both FCPM directions. However, for lower wave numbers ($k_y < 0.004 \text{ m}^{-1}$), different behaviors are observed for each velocity component, with F_{xy} reaching a faster convergence for u and v , and the CPM reaching a faster convergence for w . Overall, these differences in spectra evolution are small, and we find the performance of the CPM and the FCPM to be similar for this neutral stability case.

4.2. Convective Stability Conditions

Convective mesoscale forcing contains low levels of turbulence only present at large scales (Figure 2b). These large-scale fluctuations, along with the strong, convective forcing generate high wave number turbulent motions downstream of the inflow boundary for the unperturbed, nested case (Figure 10a), unlike the case of neutral stability conditions (Figure 4).

In the convective case, as in the neutral case, we select optimal amplitudes of the vertical (Figure 11) and horizontal (Figure 12) force perturbation based on the evolution of resolved TKE. In this case, we found that for all of the FCPM perturbation amplitudes and directions there was an overshoot of TKE, which then decreased gradually down to the asymptotic value. Based on this resolved TKE analysis, all of the force perturbation amplitudes produced very similar behaviors, which produced only slight improvements over the unperturbed case. In comparison, the CPM produced a very similar overshoot of TKE initially, but decreased to the stable value in a significantly shorter distance than the FCPM. Based on this resolved TKE analysis, the CPM produces a significantly shorter fetch than any of the force perturbation configurations, throughout all heights within the boundary layer (Figure 13). Figure 13 shows that the unperturbed case produces

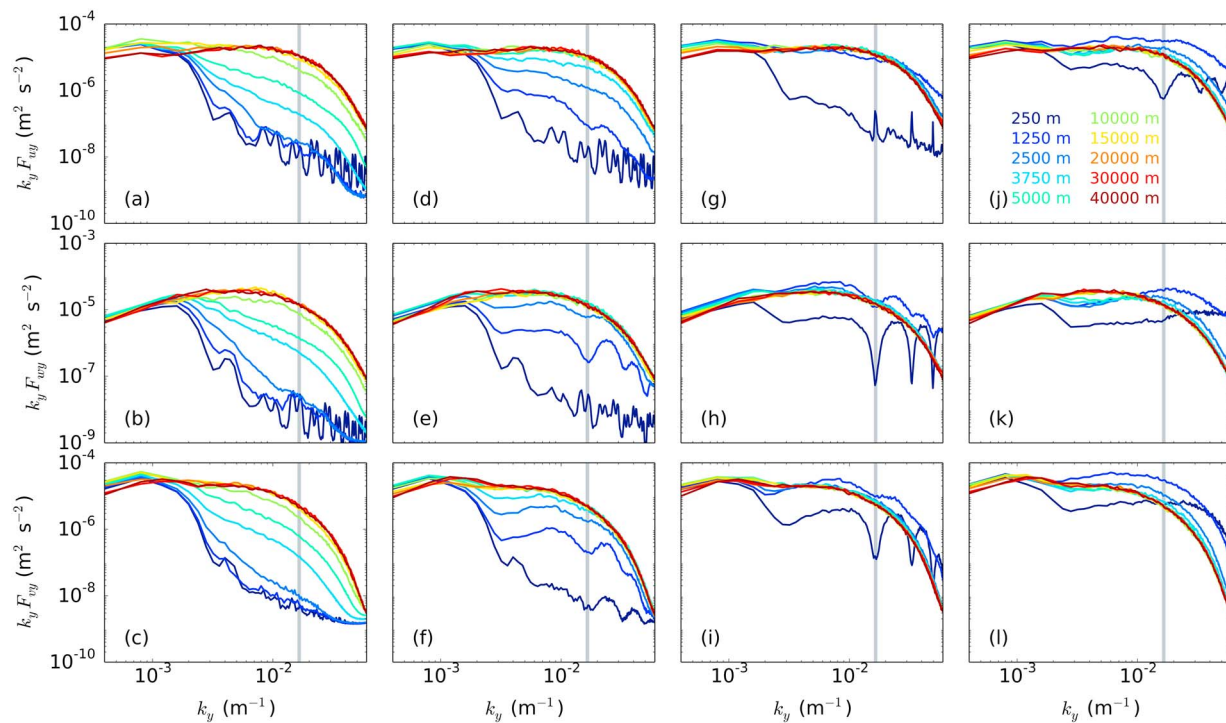


Figure 14. Time-averaged turbulent spectra of u , w , and v in the y direction for (a–c) C_{NP} , (d–f) $C_{\theta,0.33}$, and (g–i) $C_{z,10000}$, (j–l) $C_{xy,5000}$ as a function of wave number, k_y , at a height of 400 m. The vertical gray lines show the wave number corresponding to the scale of the perturbations ($8 \Delta x$).

very high levels of TKE near the surface and the top of the boundary layer, which take a long distance to dissipate. While the CPM still shows these regions of high TKE, the perturbations of θ significantly reduce their magnitude and the distance necessary for them to dissipate. However, Figures 13c and 13d show that while the force perturbations produce very high levels of TKE in the first few kilometers downstream from the inflow boundary, these high levels of TKE quickly dissipate, leading way to similar high-TKE levels near the surface and the top of the boundary layer as observed in the unperturbed and CPM cases. While these high-TKE regions are slightly weaker and shorter than for the unperturbed case, they remain significantly stronger than for the CPM.

Our results indicate the robustness of the CPM for these convective conditions. This shorter CPM fetch indicates that the strong, thermally driven motions produced by perturbations in the θ field interact more efficiently with the thermally driven mixing characteristic of the convective conditions, thus accelerating the production of fully developed turbulence. More specifically, while the FCPM will have an instantaneous effect on these strongly convective flows, the strong convective forcing will continue to dominate and will quickly dissipate the structures produced by the force perturbations. However, by using temperature perturbations (CPM) to directly perturb the stratified field driving the convective forcing, the perturbation effect will interact, rather than be overridden by the random perturbations. The shorter fetch produced by the CPM may be further improved by the use of the optimal convective scaling recently developed by Muñoz-Esparza and Kosović (2018).

For further spectral analysis we compare $C_{xy,5000}$, $C_{z,10000}$ with the CPM ($C_{\theta,0.33}$), and the unperturbed simulation. The application of the CPM introduces fluctuations in the initial θ field while having no immediate, direct effect on the velocity fields. As time steps advance, after θ perturbations are added, the wind speed reacts accordingly following the governing equations. This noninstantaneous perturbation effect can be seen for the spectra of u by comparing the line corresponding to $x = 250$ m in Figure 14a, and the same line for Figure 14d, for the spectra of w by making the same comparison for Figures 14b and 14e and for the spectra of v by comparing Figures 14c and 14f. Therefore, the effect of these perturbations on wind speed fluctuations is dependent on the rate of conversion between potential energy from temperature gradients to kinetic energy. This conversion mechanism produces a slower initial increase of turbulent motions for

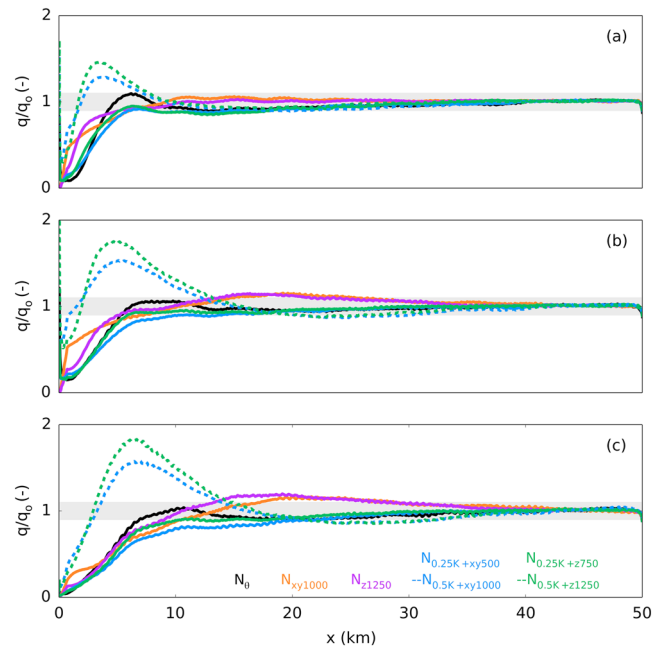


Figure 15. Time-averaged neutral boundary layer evolution of resolved turbulent kinetic energy (q), for the nested large eddy simulation forced as a function of distance downstream of the nested inflow boundary, x , at heights (a) 100, (b) 250, and (c) 350 m. At each height, q is normalized by q_0 , the mean of turbulent kinetic energy at $x = 40$ to 50 km for that specific height.

wave numbers above 0.001 m^{-1} for the first 4 km downstream of the inflow boundary, when compared with the FCPM.

Conversely, the FCPM produce an instantaneous effect on the velocity fields, resulting in a very rapid overshoot of energy across all wave numbers for the first 3 km downstream of the inflow boundary (Figures 14g–14i and 14j–14l). Despite this faster, initial triggering of turbulent motions, the additional TKE produced by the FCPM requires a longer distance to dissipate, resulting in a significantly longer fetch than the CPM. This is consistent with the evolution of TKE shown in Figure 13.

5. Combination of the FCPM and CPM

In section 4.1 we find that the FCPM generates a fetch comparable to the CPM for the neutral stability case and within a fetch comparable to the unperturbed case for the convective stability case. We find that, while the FCPM produces a faster initial increase in turbulence, it produces an overshoot in TKE, which takes a longer distance to stabilize. In contrast, the CPM produces a slower initial turbulence increase, which then takes a shorter distance to stabilize. In this section, we explore if a combination of θ and force perturbations can produce additional improvements by leveraging each method's strengths.

We test two different perturbation combinations: $F_{xy+\theta}$ and $F_{z+\theta}$ and combine half of the optimal amplitudes, as well as the full optimal values. For the neutral case, neither combination of perturbations produced clear improvement, and both perturbation combinations produced similar TKE evolution (Figure 15). Based on these tests we observed neither the quick initial increase in turbulence produced by the FCPM nor the fast decrease to a stable value produced by the CPM. For the combination of perturbations using half of the optimal amplitudes, both combined perturbations appear to trigger lower levels of TKE than the stable value, which slowly increase with fetch. This indicates that the perturbation amplitudes tested may not be strong enough. The combination of higher perturbation magnitudes produces rapid overshoots of TKE followed by a slow decrease for all of the combinations tested. Based on this, we found no additional advantage to the use of the combination of the CPM and FCPM.

A similar test is performed for the CBL case (Figure 16). Again, no obvious improvements were found for these configurations and both combination tests produced very similar results. Both perturbation combinations performed similarly to F_z , with a fast initial increase in TKE and then a slow decrease to the stable value.

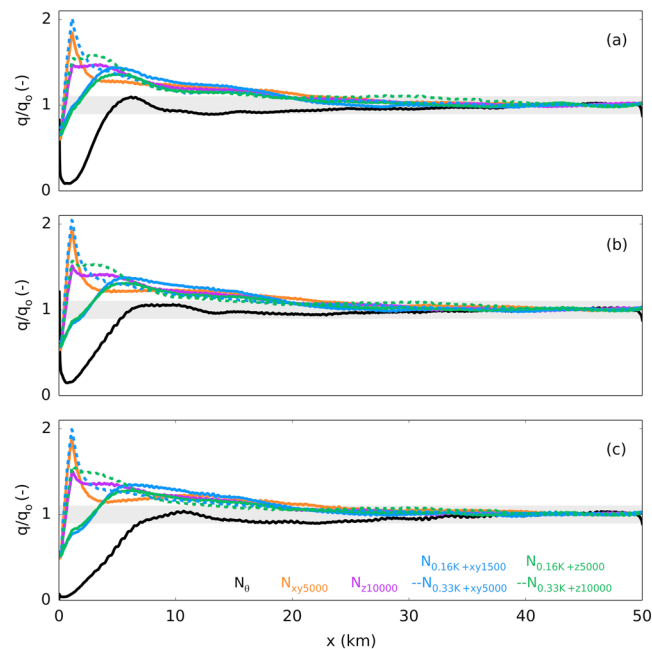


Figure 16. Time-averaged convective boundary layer evolution of resolved turbulent kinetic energy (q), for the nested large eddy simulation forced as a function of distance downstream of the nested inflow boundary, x , at heights (a) 500, (b) 1,000, and (c) 1,500 m. At each height, q is normalized by q_0 , the mean of turbulent kinetic energy at $x = 40$ to 50 km for that specific height.

This overshooting behavior was found to be particularly strong when combining perturbation methods using their full optimal amplitudes. Ultimately, both method combinations produced significantly longer fetches than the CPM.

None of the perturbation combinations and stability conditions studied here performed better than the best of its stand-alone components. It is possible that the drawbacks of each method negatively affect the final performance of the combination, while the advantages are not able to overcome these. However, the use of stronger amplitudes for all of the perturbation combinations may shed more light on the combined behavior.

6. Conclusions

As computational resources become faster and more accessible, bridging between mesoscale and microscale models is becoming more common practice for a variety of applications, from studies of wind energy production to fire propagation. The generation of highly resolved turbulence in microscale domains is a nontrivial problem that can significantly increase the cost of these simulations. In this study we implemented a new flow perturbation technique based on the CPM, by applying random, direct vertical and horizontal forces at the inflow boundaries of grid-nested, microscale domains. The spatial structure and refreshment time rate of the force perturbations was based on the CPM (Muñoz-Esparza et al., 2015). We tested the FCPM method in an idealized setting, under two atmospheric stability conditions: neutral and convective. Additionally, combinations of the FCPM and CPM were tested to assess whether further improvements can be achieved.

The FCPM was found to directly accelerate and decelerate the flow, thus removing the process of converting potential temperature gradients into kinetic energy, which was necessary for the CPM. This resulted in a faster initial development of turbulence, for short distances up to ~ 3 km downstream of the inflow boundaries. However, further downstream from the inflow boundary, the development of turbulence in the FCPM slows down, and the CPM reaches an equilibrium state faster than the FCPM. For both stability conditions, F_z perturbations performed better than F_{xy} .

For the neutral case, the performance of the FCPM is comparable to the CPM. Near the surface ($z = 100$ m), the vertical FCPM produced the shortest fetch of 5 km, while the CPM produced a fetch closer to 10 km. However, higher in the boundary layer both the vertical FCPM and the CPM produced very similar fetches of 10–15 km. For the convective case, neither FCPM direction produced a shorter fetch than the

CPM. Instead, the FCPM produced a very high overshoot of TKE near the inflow boundary, which quickly dissipated leading to a slowly evolving pattern of high TKE near the ground and the top of the BL. This slowly evolving process produced a fetch of 25–30 km which was also observed in the unperturbed case. Therefore, the FCPM produced smaller improvements over the unperturbed case, while the CPM significantly reduced the effect of these high-TKE regions, with a shorter fetch of 15–20 km.

The combination of F and θ perturbations does not improve upon the optimal, stand-alone force perturbation configurations when using half of the optimal stand-alone values. The lower-amplitude perturbation combinations tested herein generated slowly increasing levels of TKE, which produced longer fetches than any of the stand-alone perturbation tests for both stability conditions.

The force perturbations used in the FCPM have shown certain advantages over the θ perturbations used by the CPM during the initial turbulence development region. Overall, the FCPM produced comparable performance to the CPM. Based on our study, we recommend the continued use of the CPM method, which has been further developed, until clear advantages are shown from randomly perturbing different variables. These results point to the strength of the random perturbation methods, which can significantly accelerate the development of microscale turbulence irrespective of the source of the perturbations. All of the methods used in this study may produce even shorter turbulence generation fetches in the presence of complex terrain, where the terrain complexity further aids in triggering turbulence motions. Ongoing work is being performed to test the performance of the FCPM in a real simulation for a full diurnal cycle for a nearly flat terrain case. Future developments of the FCPM could involve testing the technique under a wide variety of forcing conditions to develop a more practical method for amplitude optimization, performing a more comprehensive study of the combination of the FCPM and CPM, and testing the FCPM in simulations of flows over complex-terrain.

Acknowledgments

Funding for this work was provided through the MMC project, supported at LANL by the Wind Energy Technologies Office within the U.S. Department of Energy's Office of Energy Efficiency and Renewable Energy through the Atmosphere to Electrons program. The views expressed in the article do not necessarily represent the views of the U.S. DOE, NSF, or the U.S. Government. The U.S. Government retains, and the publisher, by accepting the article for publication, acknowledges that the U.S. Government retains a nonexclusive, paid-up, irrevocable, worldwide license to publish or reproduce the published form of this work, or allow others to do so, for U.S. Government purposes. Computing resources were provided by the LANL Institutional Computing Program through the W17_atmo_turbulence project. J. K. L.'s effort was supported by the National Science Foundation under AGS-1565498. Data storage is supported by the University of Colorado Boulder "PetaLibrary". All the data used in this study are stored in a github repository, accessible through this link (https://github.com/orazzamarual/perts_figures).

References

- Araya, G., Castillo, L., Meneveau, C., & Jansen, K. (2011). A dynamic multi-scale approach for turbulent inflow boundary conditions in spatially developing flows. *Journal of Fluid Mechanics*, *670*, 581–605. <https://doi.org/10.1017/S0022112010005616>
- Archer, C. L., Mirzaeisefat, S., & Lee, S. (2013). Quantifying the sensitivity of wind farm performance to array layout options using large-eddy simulation. *Geophysical Research Letters*, *40*, 4963–4970. <https://doi.org/10.1002/grl.50911>
- Beare, R. J. (2013). A length scale defining partially-resolved boundary layer turbulence simulations. *Boundary-Layer Meteorology*, *151*(1), 39–55. <https://doi.org/10.1007/s10546-013-9881-3>
- Bhaganagar, K., & Debnath, M. (2014). Implications of stably stratified atmospheric boundary layer turbulence on the near-wake structure of wind turbines. *Energies*, *7*(9), 5740–5763. <https://doi.org/10.3390/en7095740>
- Ching, J. R., Rotunno, M., LeMone, A., Martilli, B., Kosović, B., Jimenez, P. A., & Dudhia, J. (2014). Convectively induced secondary circulations in fine-grid mesoscale numerical weather prediction models. *Monthly Weather Review*, *142*(9), 3284–3302. <https://doi.org/10.1175/MWR-D-13-00318.1>
- Chow, F. K., Schär, C., Ban, N., Lundquist, K. A., Schlemmer, L., & Shi, X.-M. (2019). Crossing multiple gray zones in the transition from mesoscale to microscale simulation over complex terrain. *Atmosphere*, *10*, 274. <https://doi.org/10.3390/atmos10050274>
- Deardorff, J. W. (1972). Numerical investigation of neutral and unstable planetary boundary layers. *Journal of the Atmospheric Sciences*, *29*(1), 91–115. [https://doi.org/10.1175/1520-0469\(1972\)029<0091:NIONAU>2.0.CO;2](https://doi.org/10.1175/1520-0469(1972)029<0091:NIONAU>2.0.CO;2)
- Deardorff, J. W. (1980). Stratocumulus-capped mixed layers derived from a three-dimensional model. *Boundary-Layer Meteorology*, *18*, 495–527. <https://doi.org/10.1007/BF00119502>
- di Mare, L., Klein, M., Jones, W. P., & Janicka, J. (2006). Synthetic turbulence inflow conditions for large-eddy simulation. *Physics of Fluids*, *18*(2), 25107. <https://doi.org/10.1063/1.2130744>
- Fang, J., & Porté-Agel, F. (2015). Large-eddy simulation of very-large-scale motions in the neutrally stratified atmospheric boundary layer. *Boundary-Layer Meteorology*, *155*, 397–416. <https://doi.org/10.1007/s10546-015-0006-z>
- Honnert, R., Masson, V., & Couvreur, F. (2011). A diagnostic for evaluating the representation of turbulence in atmospheric models at the kilometer scale. *Journal of the Atmospheric Sciences*, *68*(12), 3112–3131. <https://doi.org/10.1175/JAS-D-11-061.1>
- Jähn, M., Muñoz-Esparza, D., Chouza, F., Reitebuch, O., Knoth, O., Haari, M., & Ansmann, A. (2016). Investigations of boundary layer structure, cloud characteristics and vertical mixing of aerosols at Barbados with large eddy simulations. *Atmospheric Chemistry and Physics*, *16*(2), 651–674. <https://doi.org/10.5194/acp-16-651-2016>
- Jimenez, P. A., Dudhia, J., González-Rouco, J. F., Navarro, J., Montávez, J. P., & García-Bustamante, E. (2012). A revised scheme for the WRF surface layer formulation. *Monthly Weather Review*, *140*, 898–918. <https://doi.org/10.1175/MWR-D-11-00056.1>
- Keating, A., Piomelli, U., Balaras, E., & Kaltenbach, H.-J. (2014). A priori and a posteriori tests of inflow conditions for large-eddy simulation. *Physics of Fluids*, *16*, 4696–4712. <https://doi.org/10.1063/1.1811672>
- Klein, M., Sadiki, A., & Janicka, J. (2003). A digital filter based generation of inflow data for spatially developing direct numerical or large eddy simulations. *Physics of Fluids*, *15*(2), 652–665. [https://doi.org/10.1016/S0021-9991\(03\)00090-1](https://doi.org/10.1016/S0021-9991(03)00090-1)
- Klemp, J. B., Dudhia, J., & Hassiotis, A. D. (2008). An upper gravity-wave absorbing layer for NWP applications. *Monthly Weather Review*, *136*(10), 3987–4004. <https://doi.org/10.1175/2008MWR2596.1>
- Kondo, K., Murakami, S., & Mochida, A. (1997). Generation of velocity fluctuations for inflow boundary condition of LES. *Journal of Wind Engineering and Industrial Aerodynamics*, *68–69*, 51–64. [https://doi.org/10.1016/S0167-6105\(97\)00062-7](https://doi.org/10.1016/S0167-6105(97)00062-7)
- Kosović, B. (1997). Subgrid-scale modelling for the large-eddy simulation of high-reynolds-number boundary layers. *Journal of Fluid Mechanics*, *336*, 151–182. <https://doi.org/10.1017/S0022112096004697>

- Le, H., Moin, P., & Kim, J. (1997). Direct numerical simulation of turbulent flow over a backward-facing step. *Journal of Fluid Mechanics*, 330, 349–374. <https://doi.org/10.1017/S0022112096003941>
- Lee, S., Lele, S., & Moin, P. (1992). Simulation of spatially evolving compressible turbulence and the application of Taylors hypothesis. *Physics of Fluids*, 4(7), 1521–1530. <https://doi.org/10.1063/1.858425>
- Liu, Y., Warner, T., Liu, Y., Vincent, C., Wi, W., Mahoney, B., et al. (2011). Simultaneous nested modeling from the synoptic scale to the LES scale for wind energy applications. *Journal of Wind Engineering and Industrial Aerodynamics*, 99(4), 308–319. <https://doi.org/10.1016/j.jweia.2011.01.013>
- Lund, T. S., Wu, X., & Squires, K. (1998). Generation of turbulent inflow data for spatially-developing boundary layer simulations. *Journal of Computational Physics*, 140(2), 233–258. <https://doi.org/10.1006/jcph.1998.5882>
- Matheou, G., Chung, D., Nuijens, L., Stevens, B., & Teixeira, J. (2011). On the fidelity of large-eddy simulation of shallow precipitating cumulus convection. *Monthly Weather Review*, 139, 2918–2939. <https://doi.org/10.1175/2011MWR3599.1>
- Mayor, S. D., Spalart, P. R., & Tripoli, G. J. (2002). Application of a perturbation recycling method in the large-eddy simulation of a mesoscale convective internal boundary layer. *Journal of the Atmospheric Sciences*, 59(15), 2385–2395. [https://doi.org/10.1175/1520-0469\(2002\)059<2385:AOAPRM>2.0.CO;2](https://doi.org/10.1175/1520-0469(2002)059<2385:AOAPRM>2.0.CO;2)
- Mazzaro, L. J., Muñoz-Esparza, D., Lundquist, J. K., & Linn, R. R. (2017). Nested mesoscale-to-LES modeling of the atmospheric boundary layer in the presence of under-resolved convective structures. *Journal of Advances in Modeling Earth Systems*, 9, 1795–1810. <https://doi.org/10.1002/2017MS000912>
- Mirocha, J., Kosović, B., & Kirkil, G. (2014). Resolved turbulence characteristics in large-eddy simulations nested within mesoscale simulations using the weather research and forecasting model. *Monthly Weather Review*, 142(2), 806–831. <https://doi.org/10.1175/MWR-D-13-00064.1>
- Mirocha, J. D., Lundquist, J. K., & Kosović, B. (2010). Implementation of a nonlinear subfilter turbulence stress model for large-eddy simulation in the advanced research WRF Model. *Monthly Weather Review*, 138(11), 4212–4228. <https://doi.org/10.1175/2010MWR3286.1>
- Moeng, C.-H., & Sullivan, P. (1994). A comparison of shear- and buoyancy-driven planetary boundary layer flows. *Journal of the Atmospheric Sciences*, 51(7), 999–1022. [https://doi.org/10.1175/1520-0469\(1994\)051<0999:ACOSAB>2.0.CO;2](https://doi.org/10.1175/1520-0469(1994)051<0999:ACOSAB>2.0.CO;2)
- Moeng, C.-H., & Wyngaard, J. C. (1994). Statistics of conservative scalars in the convective boundary layer. *Journal of the Atmospheric Sciences*, 41(21), 3161–3169. [https://doi.org/10.1175/1520-0469\(1984\)041<3161:SOCSTI>2.0.CO;2](https://doi.org/10.1175/1520-0469(1984)041<3161:SOCSTI>2.0.CO;2)
- Monin, A. S., & Obukhov, A. M. (1954). Basic turbulence mixing laws in the atmospheric surface layer. *Tr. Inst. Teor. Geofiz., Akad. Nauk SSSR* 24, 151, 163–187. <https://doi.org/10.1007/s10546-015-0045-5>
- Morgan, B., Larsson, J., Kawai, S., & Lele, S. K. (2011). Improving low-frequency characteristics of recycling/rescaling inflow turbulence generation. *AIAA Journal*, 49(3), 582–597. <https://doi.org/10.2514/1.J050705>
- Muñoz-Esparza, D., & Kosović, B. (2018). Generation of inflow turbulence in large-eddy simulations of nonneutral atmospheric boundary layers with the cell perturbation method. *Monthly Weather Review*, 146, 1889–1909. <https://doi.org/10.1175/MWR-D-18-0077.1>
- Muñoz-Esparza, D., Kosović, B., Garcia-Sanchez, C., & Beeck, J. (2014). Nesting turbulence in an offshore convective boundary layer using large-eddy simulations. *Boundary-Layer Meteorology*, 151(3), 453–478. <https://doi.org/10.1007/s10546-014-9911-9>
- Muñoz-Esparza, D., Kosović, B., Mirocha, J., & Beeck, J. (2014). Bridging the transition from mesoscale to microscale turbulence in numerical weather prediction models. *Boundary-Layer Meteorology*, 153(3), 409–440. <https://doi.org/10.1007/s10546-014-9956-9>
- Muñoz-Esparza, D., Kosović, B., Mirocha, J., & Beeck, J. (2015). A stochastic perturbation method to generate inflow turbulence in large-eddy simulation models: Application to neutrally stratified atmospheric boundary layers. *Phys. Fluids*, 27(3), 035102. <https://doi.org/10.1063/1.4913572>
- Muñoz-Esparza, D., Sauer, J. A., Linn, R. R., & Kosović, B. (2016). Limitations of one-dimensional mesoscale PBL parameterizations in reproducing mountain-wave flows. *Journal of the Atmospheric Sciences*, 73(7), 2603–2614. <https://doi.org/10.1175/JAS-D-15-0304.1>
- Muñoz-Esparza, D., Sauer, J. A., Linn, R. R., & Kosović, B. (2017). Coupled mesoscale-LES modeling of a diurnal cycle during the CWEX-13 field campaign: From weather to boundary-layer eddies. *Journal of Advances in Modeling Earth Systems*, 9, 1572–1594. <https://doi.org/10.1002/asl.377>
- Nakanishi, M., & Niino, M. (2009). Development of an improved turbulence closure model for the atmospheric boundary layer. *Journal of the Meteorological Society of Japan*, 87(5), 895–912. <https://doi.org/10.2151/jmsj.87.895>
- Nakayama, H., Takemi, T., & Nagai, H. (2012). Large-eddy simulation of urban boundary-layer flows by generating turbulent inflows from mesoscale meteorological simulations. *Atmospheric Science Letters*, 13(3), 180–186. <https://doi.org/10.1002/2017MS000960>
- Pamies, M., Weiss, P.-E., Garnier, E., Deck, S., & Sagaut, P. (2009). Generation of synthetic turbulent inflow data for large eddy simulation of spatially evolving wall-bounded flows. *Physics of Fluids*, 21(4), 045103. <https://doi.org/10.1063/1.3103881>
- Poletto, R., Craft, T., & Revell, A. (2013). A new divergence free synthetic eddy method for the reproduction of inlet flow conditions for LES. *Flow, Turbulence and Combustion*, 91(3), 519–539. <https://doi.org/10.1007/s10494-013-9488-2>
- Rai, R. K., Berg, L. K., Kosović, B., Mirocha, J. D., Pekour, M. S., & Shaw, W. J. (2016). Comparison of measured and numerically simulated turbulence statistics in a convective boundary layer over complex terrain. *Boundary-Layer Meteorology*, 163(1), 69–89. <https://doi.org/10.1007/s10546-016-0217-y>
- Sauer, J. A., Muñoz-Esparza, D., Canfield, J. M., Costigan, K. R., Linn, R. R., & Kim, Y.-J. (2016). A large-eddy simulation study of atmospheric boundary layer influence on stratified flows over terrain. *Journal of the Atmospheric Sciences*, 73(7), 2615–2632. <https://doi.org/10.1175/JAS-D-15-0282.1>
- Schalkwijk, J., Harmen, J. J., Jonker, A., Bosveld, P., & Siebesma, F. C. (2015). A year-long large-eddy simulation of the weather over Cabauw: An overview. *Monthly Weather Review*, 143(3), 828–844. <https://doi.org/10.1175/MWR-D-14-00293.1>
- Seifert, A., & Heus, T. (2013). Large-eddy simulation of organized precipitating trade wind cumulus clouds. *Atmospheric Chemistry and Physics*, 13, 5631–5645. <https://doi.org/10.5194/acp-13-5631-2013>
- Shin, H. H., & Dudhia, J. (2016). Evaluation of PBL parameterizations in WRF at subkilometer grid spacings: turbulent statistics in the dry convective boundary layer. *Monthly Weather Review*, 144(3), 1161–1177. <https://doi.org/10.1175/MWR-D-15-0208.1>
- Skamarock, W. C., Klemp, J. B., Dudhia, J., Gill, D. O., Barker, D. M., Duda, M. G., et al. (2008). A description of the advanced research WRF version 3 (NCAR/TN-475+STR): NCAR Technical Note. Boulder, CO. <https://doi.org/10.1175/MWR2830.1>
- Smith, C. M., & Skyllingstad, E. D. (2009). Investigation of upstream boundary layer influence on mountain wave breaking and lee wave rotors using a large-eddy simulation. *Journal of the Atmospheric Sciences*, 66, 3147–3164. <https://doi.org/10.1175/2009JAS2949.1>
- Spille-Kofoff, A., & Kaltenbach, H. J. (2001). Generation of turbulent inflow data with a prescribed shear-stress profile. DNS/LES Progress and Challenges, 8.
- Tabor, G. R., & Baba-Ahmadi, M. H. (2010). Inlet conditions for large eddy simulation: A review. *Computers and Fluids*, 39(4), 553–567. <https://doi.org/10.1016/j.compfluid.2009.10.007>

- Talbot, C., Bou-Zeid, E., & Smith, J. (2012). Nested mesoscale large-eddy simulations with WRF: Performance in real test cases. *Journal of Hydrometeorology*, *13*(5), 1421–1441. <https://doi.org/10.1175/JHM-D-11-048.1>
- Vanderwende, B. J., Kosović, B., Lundquist, J. K., & Mirocha, J. D. (2016). Simulating effects of a wind-turbine array using LES and RANS. *Journal for Advances in Modeling Earth Systems*, *8*, 1376–1390. <https://doi.org/10.1002/2016MS000652>
- Vollmer, L., van Dooren, M., Trabucchi, D., Schneemann, J., Steinfeld, G., Witha, B., et al. (2015). First comparison of LES of an offshore wind turbine wake with dual-Doppler lidar measurements in a German offshore wind farm. *Journal of Physics: Conference Series*, *625*, 012001. <https://doi.org/10.1088/1742-6596/625/1/012001>
- Wyngaard, J. C. (2004). Toward numerical modeling in the "terra incognita". *Journal of the Atmospheric Sciences*, *61*(14), 1816–1826. [https://doi.org/10.1175/1520-0469\(2004\)061<1816:TNMITT>2.0.CO;2](https://doi.org/10.1175/1520-0469(2004)061<1816:TNMITT>2.0.CO;2)
- Xie, Z.-T., & Castro, I. P. (2008). Efficient generation of inflow conditions for large eddy simulation of street-scale flows. *Flow, Turbulence and Combustion*, *81*(3), 449–470. <https://doi.org/10.1007/s10494-008-9151-5>
- Zajackowski, F. J., Haupt, S. E. E., & Schmehl, K. J. (2011). Thea preliminary study of assimilating numerical weather prediction data into computational fluid dynamics models for wind prediction. *Journal of Wind Engineering and Industrial Aerodynamics*, *99*, 320–329. <https://doi.org/10.1016/j.jweia.2011.01.023>
- Zhou, B., & Chow, F. K. (2013). Nighttime turbulent events in a steep valley: A nested large-eddy simulation study.0. *Journal of the Atmospheric Sciences*, *70*(10), 3262–3276. <https://doi.org/10.1175/JAS-D-13-02.1>
- Zhou, B., Simon, J. S., & Chow, F. K. (2014). The convective boundary layer in the terra incognita. *Journal of the Atmospheric Sciences*, *71*(7), 2545–2563. <https://doi.org/10.1175/JAS-D-13-0356.1>